Carbon-Capped PtNi Catalysts for the Oxygen Reduction Reaction in Acidic Environment: A Durability Study

Quentin Labarde, Andres O Godoy, Laetitia Dubau, Fabrice Micoud, Marian Chatenet

Carbon-capped PtNi catalysts for the oxygen reduction reaction in acidic environment: A durability study

Quentin Labarde[1-2], Andres O. Godoy[3], Laetitia Dubau[1], Fabrice Micoud[2], Marian Chatenet[1,*]

[1] Univ. Grenoble Alpes, Univ. Savoie Mont Blanc, CNRS, Grenoble INP*, LEPMI, 38000 Grenoble, France

*Institute of Engineering and Management Univ. Grenoble Alpes

[2] Univ. Grenoble Alpes, CEA, LITEN, 38000 Grenoble, France

[3] Center of Clean Energy Engineering, Institute of Materials Science University of Connecticut 44 Weaver Rd, Unit 5233, Storrs, USA

[*] Marian.Chatenet@grenoble-inp.fr

Abstract

Protective-shell catalysts (particularly carbon-capped catalysts), may increase the durability of oxygen reduction catalysts, owing to their supposed anti-degradation effect. The mechanisms promoting this effect are still questioned and further scientific scrutiny is needed to better understand their underlying principle. In this paper, three carbon-capped PtNi/C catalysts with different extents of carbon cap graphitization were synthesized *via* a one-pot heat-treatment. A precise electrochemical activation was applied, leading to similar intrinsic ORR activity than for a commercial Pt_3Ni/VC benchmark catalyst and larger activity than for the mother Pt/Gr.C catalyst. To examine their robustness once fully activated, an aggressive accelerated stress test (AST) in an electrochemical half-cell, which emphasizes Pt dissolution/redeposition was performed and coupled with *post mortem* analyses. The carbon-capped catalyst with the most graphitized shell is able to withstand the AST: its Pt nanoparticle size is less affected than for uncapped catalysts, suggesting a positive action of the protective carbon cap.

Keywords

Proton exchange membrane fuel cell (PEMFC), Oxygen reduction reaction (ORR), PtNi alloy catalysts, Carbon-capped catalysts, Accelerated stress tests (AST).

1. Introduction

Proton-exchange-membrane fuel cells (PEMFCs) are to date the most promising fuel cell technology; its readiness level makes it compatible with large-scale commercialization within the next decade. In that effort, the interest for PEMFC systems has recently shifted from Light Duty Vehicles (LD*Vs*) to Heavy Duty Vehicles (HD*Vs*), bringing new technical challenges, *e.g.* higher efficiency and long-term durability (up to 30 000 hours) [1]. Membrane-Electrode Assembly (MEA) degradation has always been the subject of many research works and the multiple mechanisms at stake are summarized in recent reviews [2,3]. In particular, catalysts degradation caused by nanoparticles (NPs) growth due to electrochemical Oswald ripening and electrochemical dissolution-redeposition processes (as well as NPs agglomeration/detachment induced by carbon corrosion) both yield Electrochemically Active Surface Area (ECSA) loss and the progressive dwindling of the power density along the life-span of the cell. These mechanisms are more pronounced at the cathode, where the oxygen reduction reaction (ORR) takes place, at higher potential values (with more oxidizing conditions) and relative humidity (with the production of water) than at the anode environment. While there are systematic counter-measures to mitigate the degradations (*e.g.* imposing lower average cell voltage under idling or operating conditions than at open-circuit, thanks to an appropriate Energy Management System (EMS) [4]), there is still a pressing need for improvement at the material scale. To limit the NPs growth or Pt dissolution at the material level, it is required to design more thermodynamically-stable NPs. For instance, increasing the NPs size can, despite diminishing the ECSA, leads to more stable NPs (Gibbs-Thompson effect [5]), while increased inter-particles distance can retard (or prevent) agglomeration (and possible subsequent coalescence) [3,6]. A second strategy is to design NPs with a very narrow Particle-Size Distribution (PSD) to minimize the difference in Laplace energy between NPs, thereby mitigating the Oswald ripening mechanism [7,8]. In this perspective, a strategy can be the reinforcement of atomic interactions, for example by using bimetallic NPs and especially intermetallics, obtained by alloying Pt NPs with transition metals and using proper post-treatments (*e.g.* heat-treatment) [9].
Recently, it has been proposed that a confinement effect brought by the introduction of a protective carbon shell can prevent Pt dissolution [10–21]. This protective barrier can be either inorganic (metal oxides such as TiO_2, TiN, SiO_2 or ZrO_2) or organic (carbon, derived from the decomposition of organometallic or polymer precursors) [22]. For example, Yan *et al.* [18] designed a thick and porous nitrogen-doped carbon shell coating PtNi NPs catalyst, that was able to withstand 60 000 cycles between 0.6 and 0.95 V *vs* RHE, with almost no change of the polarization curves in Membrane-Electrode Assembly (MEA) configuration. This result is indeed impressive, even though the temperature at which the test was performed was not given (at room temperature, stability is more granted [23]).

Some recent papers have highlighted an inherent trade-off between activity and durability associated with this kind of catalysts, because the shell can block the active sites, that sit underneath carbon, *i.e*. in principle not totally accessible to the reactive gases [17,24]. To address this problem, some research groups created an ultra-thin and non-dense carbon shell, resulting in ready-to-use active materials; however, these catalysts have only been tested in mild conditions [13]. An alternative strategy is to perform an activation step. This activation can be either *in situ*, *e.g.* by manipulating the oxidative of reductive gases during the heat-treatment phase [14,15], *ex situ*, *e.g. via* post-synthesis acid treatment [25], or even by *operando* electrochemical activation [24,26,27]. The problem is that most of the studies published so far, where noticeable durability improvements were obtained, were based on shifting and delaying NPs degradation, as the carbon cap initially plays a sacrificial role prior to the actual Pt NPs degradations. To date there is no consensus on whether fully activated carbon-capped catalysts, operating at their maximum intrinsic activity (*i.e*. with a porous or partial cap), can effectively prevent electrochemical Oswald ripening and further dissolution-redeposition processes from forming larger NPs, or NPs agglomeration upon spillover over the carbon support and subsequent collision/agglomeration.

In this study, we employed a synthesis strategy previously developed in our group for the design of carbon-capped catalysts for alkaline fuel cell, adapted to PEMFC materials [26,28]. Three carbon-capped catalysts, differing by the respective degree of graphitization of their outer carbon layers, were synthesized and their electrochemical behaviors compared to commercial Pt/Gr.C (Pt supported on Graphitized Carbon black support) and PtNi/VC (PtNi supported on Vulcan XC-72 Carbon black support) uncapped benchmarks. Pt supported on highly graphitized carbon black support (Pt/Gr.C) was chosen as the "mother material" of the carbon-capped catalysts, because it was the most suitable for the present synthesis protocol, which includes a heat-treatment at high temperature, that could change the nanoparticles size/shape (if they were initially small) and the morphology/porosity of the carbon support (if it was amorphous), graphitized carbon black being also more robust versus carbon corrosion in operation. In that strategy, the objective of this paper is to assess if, once fully activated (*i.e*. at maximum activity), carbon-capped catalysts really slow down the nanoparticles' degradation during a standard accelerated stress test performed in half-cell set-up. In the first part of this paper, a detailed description of the electrochemical activation procedure is discussed; this procedure is necessary to obtain fully-activated NPs. In the second part, the durability of these catalysts is evaluated through an in-house designed half-cell Accelerated Stress Test (AST), which emphasizes NPs dissolution/redeposition; coupled *post mortem* Transmission Electron Microscopy (TEM) and Particle-Size Distribution (PSD) analysis enable to link the materials' degradation to the evolution of their electrochemical performance (electrochemically active surface area and intrinsic activity).

2. Method section

2.1. Material and synthesis

The procedure to synthetize carbon-capped catalysts is based on the patent of Doan *et al.* and already presented and used in previous contributions [26,28]. Here, a commercial Pt, loaded at 30wt.% on a graphitized carbon black support (Pt/Gr.C, 30wt% Pt), is used as a template. It is manually grinded and mixed to a nickel precursor (Bis(cyclopentadienyl)Ni(II), Sigma Aldrich) with a mortar. The obtained mixture is then pyrolyzed under inert atmosphere (Ar) during a ramp of *ca.* 30°C.min^{-1} from room temperature to the selected temperature, with a 30-min hold. Three temperature targets are chosen to vary the degree of graphitization of the carbon cap: 450, 700 and 900°C, leading to carbon-capped alloy catalyst denoted as $PtNi_{cp}$/Gr.C-HT450, $PtNi_{cp}$/Gr.C-HT700 and $PtNi_{cp}$/Gr.C-HT900 respectively. The initial amounts of platinum catalyst and nickel precursor are adjusted to obtain a Pt:Ni atomic ratio of 1:1. For the sake of comparison, the commercial Pt/Gr.C used for the synthesis of capped catalysts is also chosen as a benchmark, as well as a commercial PtNi alloyed catalyst (40wt% Pt_3Ni supported on Vulcan XC-72: Pt_3Ni/VC – no PtNi catalyst supported on Gr.C is commercially available, to the authors' knowledge).

2.2. Rotating Disk Electrode characterizations

Rotating Disc Electrode (RDE) measurements are performed in a 3-electrode half-cell setup. The working electrode consists of a PEEK-based glassy carbon tip (0.196 cm²), which is mirror-polished prior drop-cast of catalyst inks. Inks are prepared by mixing the catalyst powder of interest with 3.6 mL of ultrapure water (18.2 MΩ cm, < 3 ppb total organic carbon, Millipore), 1.5 mL isopropanol (HPLC grade Fisher Chemical) and the right amount of 5 wt% Nafion® dispersion (1100EW, Sigma Aldrich) to reach a I/C ratio of 0.8 [29]. After sonication to homogenize the

solution, the ink is drop-casted on the RDE tip *via* spin-coating [30] (*ca.* 600 rpm), kept during solvents evaporation induced by a hot convective air flow. Each drop-cast consists of an aliquot of 8-10 µL, targeting 20 $\mu g_{Pt}.cm^{-2}$ as areal loading. To ensure thin film wetting and complete Pt utilization, some electrolyte is pressured and forced into the thin-film using a pump. The electrolyte is fresh 0.1 M $HClO_4$ made from 70% perchloric acid ($HClO_4$, Suprapur Supelco Merck). A commercial reversible hydrogen electrode (Hydroflex RHE from Gaskatel) placed in a Lugging capillary is used as the reference electrode. The counter electrode consists of a Pt mesh for electrochemical characterizations and glassy carbon plates for ASTs to avoid Pt redeposition. A Pt wire is connected through a capacity bridge to the RHE to reduce the electric noise. The electrochemical system was connected to a Bio-Logic potentiostat (VMP3) and operated using the EC-Lab software. For each experiments, the cell was maintained at 25°C using a thermostatic bath, and the ohmic drop was dynamically corrected at 85% to avoid over-compensation [31].

CO-stripping curves were obtained as follow: The CO was purged 6 min while the potential was held at 0.1 V *vs* RHE to adsorb one monolayer of CO. After 40 min of Ar purging to remove the excess CO, CVs were performed between 0.1 and 1.05 V *vs* RHE to electrooxidize CO; the first cycle was subtracted to the second to correct from capacitive current, and the electrooxidation charge density of Pt is taken equal to 420 $\mu C.cm^{-2}$ for ECSA calculation. For the ECSA calculated from H_{upd} desorption, a charge of 210 $\mu C.cm^{-2}$ was taken.

All ORR curves were recorded at 20 $mV.s^{-1}$ in O_2-saturated electrolyte between 0.2 and 1.05 V *vs* RHE at an electrode rotation of 1600 rpm. To calculate the mass activity at 0.9 V *vs* RHE, the ORR curve was subtracted by a Pseudo-ORR (Ar-saturated 1600 rpm, noted pORR) to correct from capacitive current, and the obtained faradic current at 0.9 V *vs* RHE was corrected from mass-transport limited current at 0.4 V *vs* RHE using Koutecky-Levich equation.

2.3. Transmission Electron Microscopy and X-Ray Energy Dispersive Spectroscopy

TEM-EDS analyses were carried out using a JEOL 2010 TEM instrument operating at 200 kV acceleration voltage, with a LaB_6 filament, and a point-to-point resolution of 0.19 nm. For PSD measurements, catalysts powders were sonicated in IPA and deposited on Cu-Lacey-carbon grid as it gives rise to more attached NPs. For high magnification TEM images, the dry catalyst powder was directly deposited on the grid to avoid hydrocarbon contamination which would false carbon cap visualization.

2.4. X-Ray Diffraction

X-Ray diffraction patterns were obtained using synchrotron radiation (0.0165 nm), in transmission mode through a 700 µm Kapton capillary. The signal was collected by a Dectris Pilatus CdTe 2 M detector. A standard CeO_2 powder was used for calibration. The crystallite size was calculated by the Scherrer equation applied at the 5 firsts peaks and using 0.94 shape coefficient.

3. Results and discussion

3.1. Results of synthesis

The carbon-capped catalysts are prepared by mixing a commercial catalyst (30 wt% Pt NPs supported on a graphitized carbon black: Pt/Gr.C) with a Ni-based organometallic compound, followed by a Heat-Treatment (HT) step, as detailed in section Method-synthesis. Figure 1 illustrates the formation of the capped PtNi alloy catalysts during the HT phase. At first, the nickel precursor, namely bis(cyclopentadienyl)Ni(II), undergoes a thermal decomposition at a relatively low temperature (*ca.* 150°C), as witnessed in TGA curves (see figure S1). It is assumed that its decomposition leads to the adsorption of Ni and cyclopentadienyl rings onto the Pt NPs, followed by a disproportionation/complete decomposition reaction that terminates into carbon and Ni atoms only surrounding the Pt NPs [32,33]. Then, above *ca.* 350°C, the Ni atoms diffuse inside the Pt lattice to form a substitutional solid solution, according to the Pt-Ni nano-alloy phase diagram [34]. In this study, a Pt:Ni atomic ratio of 1:1 was targeted, to ensure sufficient amount of carbon to cover all the NPs. Finally, the ability of Ni to catalyze the graphitization of the carbon shell by the so-called layer-exchange mechanism (starting around 600°C), was used [35,36]. The 30wt% Pt/Gr.C commercial catalyst was used as a template for the carbon-capped catalysts, because it is prone to withstand the heat-treatment due to its initial NPs size (ca. 5-6 nm, see below), its loading (with long inter-particle distance), and its robust graphitic carbon support with low specific surface area and porosity [37]. Moreover, all the NPs are located at the surface of the carbon support, facilitating the interaction with the Ni precursor, hence the formation of carbon-capped PtNi alloyed NPs. Finally, a rapid heating ramp (30°C/min) and a brief duration HT holding temperature step (30 min) were used. This approach is enough to fully decompose the chelate used to form the carbon cap, while at the same time minimize crystallite growth [38]. In particular, it must be emphasized that it was on purpose decided to avoid using a carbon-cap precursor that decomposes at higher temperature (*e.g*. like Metal-Organic Frameworks (MOFs) or multidendate complexes), because high-temperature decomposition makes it more difficult to control the NPs growth and the carbon cap graphitization.

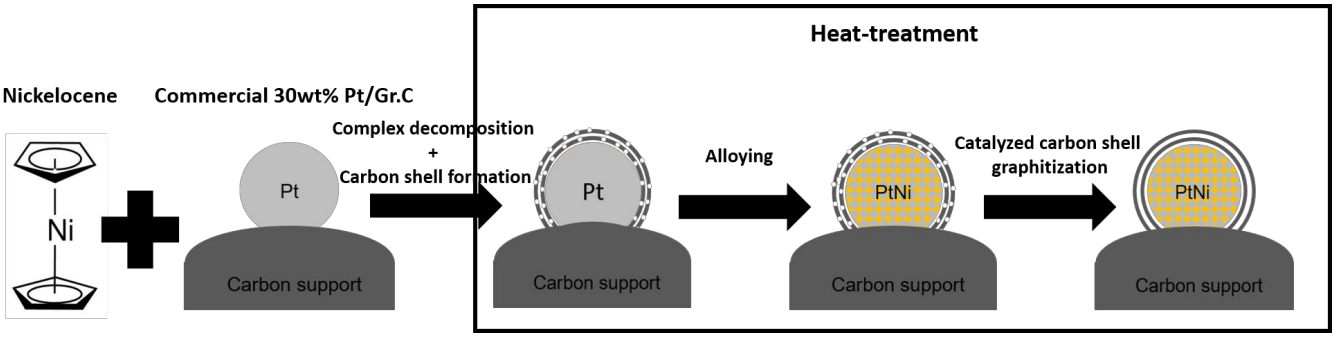

Figure 1: Schematic illustration of the carbon-capped PtNi alloy formation through one-pot pyrolysis synthesis under inert atmosphere, starting from Pt/Gr.C and an organometallic Ni-precursor.

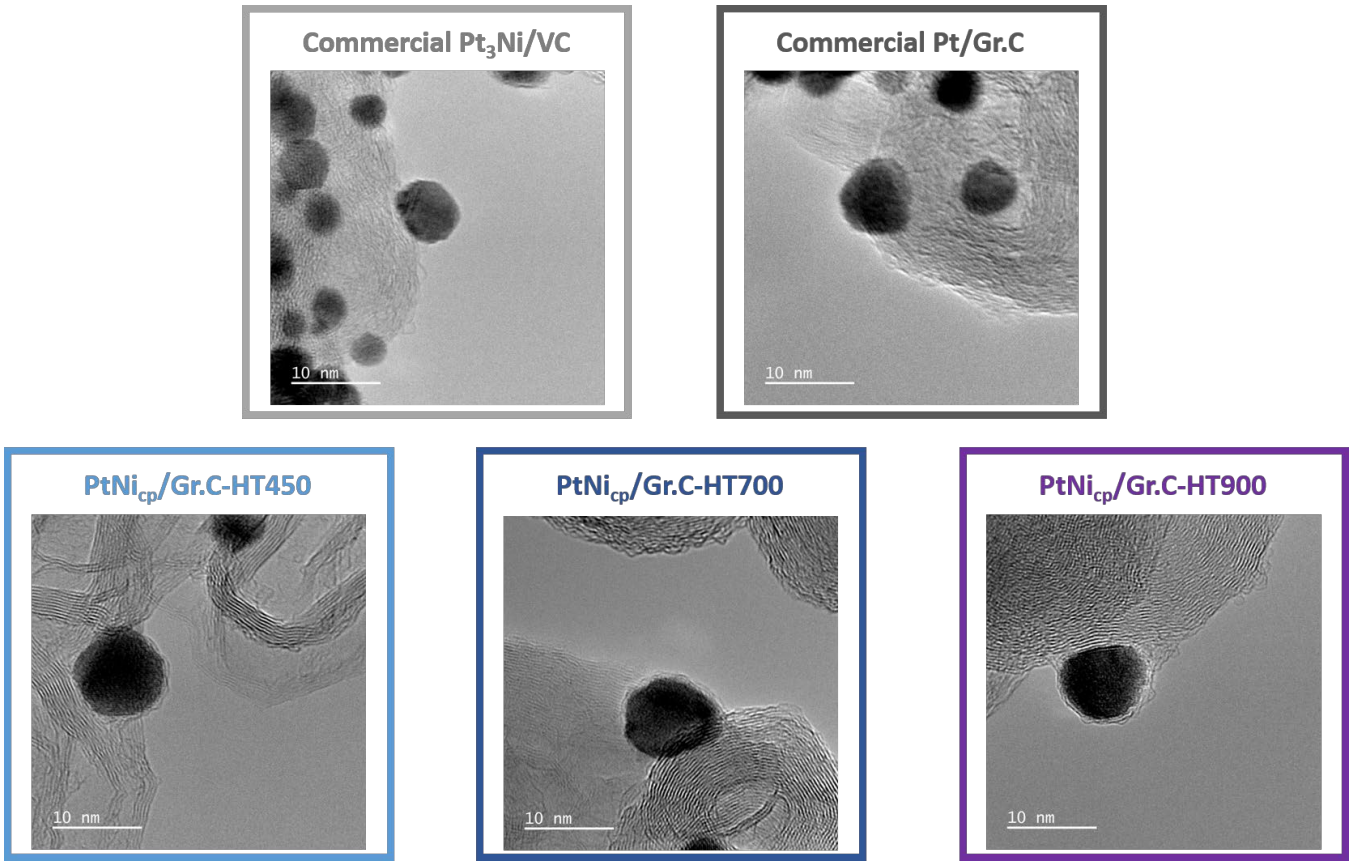

Figure 2: TEM micrograph of the two commercial benchmarks and the three synthesized carbon-capped PtNi/Gr.C catalysts, showing the presence of the carbon shell for the three latter materials.

The three catalysts synthesized were labeled $PtNi_{cp}$/Gr.C-HT450, $PtNi_{cp}$/Gr.C-HT700 and $PtNi_{cp}$/Gr.C-HT900, according to the nickel complex used (cyclopentadienyl, noted "cp", also called nickelocene) and their respective HT temperatures (450, 700 and 900°C). The TEM micrographs of Figure 2 present representative micrographs of the as-obtained catalysts, alongside the two benchmarks materials selected in this study. While the two benchmarks show no carbon cap, the three catalysts synthesized display a thin carbon cap of *ca.* 0.5-1 nm surrounding the PtNi NPs. In Figure S2 are presented low magnification TEM images with Particle Size distribution (PSD) histograms, that enable to assess the influence of the heat-treatment on the NPs sintering. It is evident that even for the highest temperature heat-treatment (900°C), the nanoparticles mean diameters are *ca.* 5 to 6 nm, hence remain very close to the particle size of the commercial Pt/Gr.C (5.1 nm) (the mother catalyst of the carbon-capped materials) and Pt_3Ni/VC (5.3 nm) catalysts. Considering the incorporation of 1 atom of Ni for each Pt atom, the size increase can be considered small (even though non-negligible) and in any case unlikely to significantly affect the particle size-related degradation during the AST and particle size effect in ORR catalysis [39]. The commercial Pt_3Ni/VC, supported on Vulcan XC-72 carbon (less graphitized than the carbon support of the four other catalysts), shall enable to evaluate if the carbon corrosion is significant during the durability test of this study. Moreover, this catalyst allows comparison with PtNi NPs, known to increase ORR activity versus Pt [40]. In any case, the overall morphology of the carbon-capped PtNi catalysts remains very close to that of the Pt/Gr.C benchmark and their composition and particle size is also similar to that of the Pt_3Ni/VC, thereby easing the comparison of their electrochemical properties.

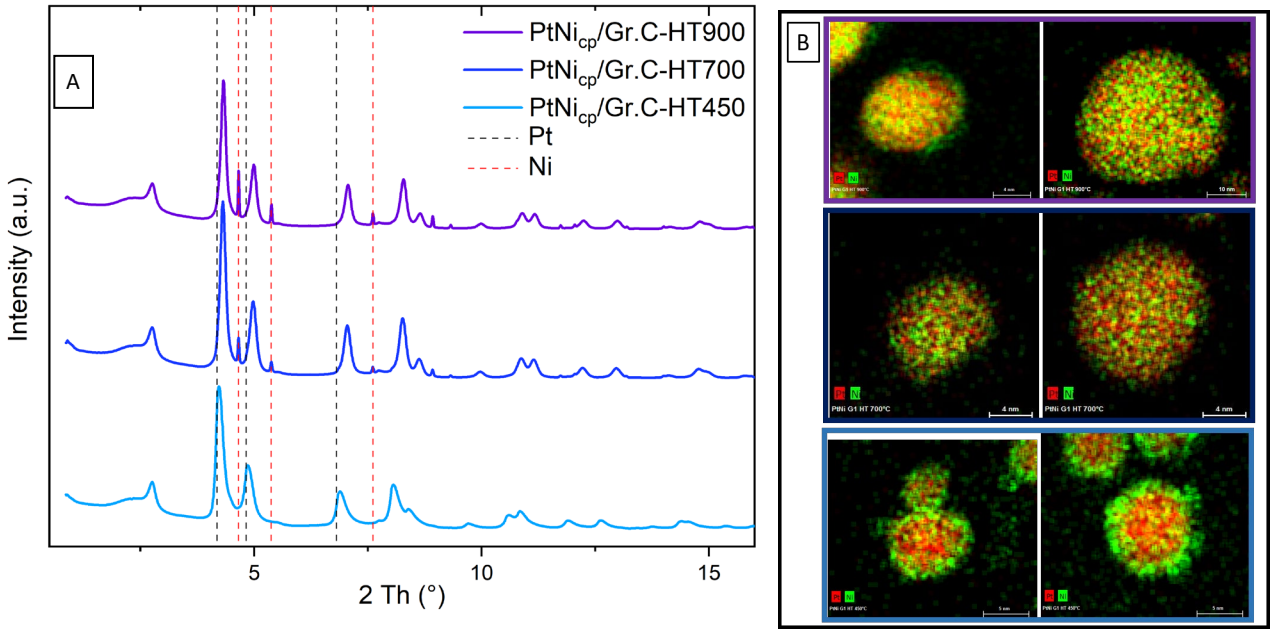

<u>Figure 3:</u> (A) X-Ray diffraction pattern for the three synthesized carbon-capped PtNi/Gr.C electrocatalysts and (B) their representative STEM-EDS-Mapping micrographs for two different particles (Pt represented in red, Ni in green).

Figure 3-A represents X-ray diffraction patterns for the three synthesized catalysts. The peak at *ca.* 3° corresponds to the graphitized carbon support (200). Peaks in-between Pt and Ni pure phases (in black and red dash lines respectively) are observed for the three materials, confirming the formation of a PtNi alloy during the HT. XRD patterns of benchmarks Pt/Gr.C and Pt_3Ni/VC are reported in Figure S4. Interestingly, for the three materials a Ni phase is (minorly) observed, which has not been noticed from a local technique like electron microscopy. It can be suggested that the blending procedure, involving mortar hand-mixing of the Pt/C and the Ni precursor, leads to a non-homogenous mixing and that Ni atoms may agglomerate and grow into isolated nanoparticles during the heat-treatment. This however appears quite marginal. Using Scherrer equation (see section method), the mean crystallites sizes are calculated to be 3.4, 4.8 and 5.2 nm, for the catalysts synthesized at 450, 700 and 900°C respectively. This was anticipated after such HT and assuming the polycrystallinity of the NPs (especially at the lowest temperature of HT). According to Vegard's law, the Pt:Ni alloy phase stoichiometry is *ca.* $Pt_{85}Ni_{15}$, $Pt_{60}Ni_{40}$, $Pt_{60}Ni_{40}$ for PtNi$_{cp}$/Gr.C-HT450, PtNi$_{cp}$/Gr.C-HT700 and PtNi$_{cp}$/Gr.C-HT900 respectively. These results confirm that a heat-treatment of 30 min at 450°C is not long enough for the Ni to diffuse inside the Pt lattice for NPs of *ca*. 5 nm. Remarkably, the diffractogram of the catalyst treated at 450°C displays asymmetric peaks, with a tail at higher angles, suggesting an angular lattice parameter shift.

STEM-EDS mapping was acquired to confirm the incorporation of Ni into the Pt phase, and to further investigate the diffraction behavior of PtNi$_{cp}$/Gr.C-HT450. EDS-mapping of Pt and Ni atoms are displayed in Figure 3-B, for the three capped catalysts. While the catalysts treated at 700 and 900°C show homogenous Ni incorporation into the pre-existing Pt NPs, the one treated at 450°C shows a Ni-rich outer shell, which can explain the XRD diffraction pattern. Local EDS analysis of the particular NPs shown in Figure 3-B indicate a Pt:Ni ratio of $Pt_{60}Ni_{40}$ for PtNi$_{cp}$/Gr.C-HT450, taking into account the non-alloyed Ni shell, similar to what XRD suggested for the two other catalysts. Therefore, it can be concluded that for the carbon-capped catalysts synthesized, around 20 at.% of the Ni coming from the precursor is far away from the Pt NPs, due to non-homogenous blending, and the other 80% are close to the Pt NPs, either partially alloyed for the sample treated at 450°C and completely alloyed for the ones treated at 700 and 900°C.

To conclude on the synthesis part, three carbon-capped catalysts were synthesized. The one synthesized at 450°C shows a core-shell structure with a higher concentration of Ni at the outer layers of Pt NPs, whereas the catalysts synthesized at 700 and 900°C show homogenous PtNi solid solutions. The degree of graphitization of the carbon cap was varied by the HT temperature and its influence on electrochemical activity and durability can be evaluated, as attempted hereafter.

3.2. Electrochemical activation

After the encapsulation of the PtNi NPs by carbon layers with different degrees of graphitization, their electrochemical characteristics were investigated in classical 3-electrode cell in Ar-saturated 0.1 M $HClO_4$ electrolyte. As mentioned in the introduction, an activation step is required if the carbon cap of the catalysts is dense enough. Here, sets of 200 potential cycles were applied, at 500 mV s^{-1} to limit the experiment duration, and the upper limit potential (UPL) was progressively increased from 1.2 up to 1.8 V *vs* RHE. After each set of 200 cycles at a given UPL value, a slower cyclic voltammogram (CV) at 20 mV s^{-1} is carried out prior to the next 200 cycles for the following UPL. This procedure allows a precise determination of the activation degree, by monitoring the coulometry related to Hydrogen under-potential deposition (H_{upd}, 0.05-0.4 V *vs* RHE) as a reliable probe to monitor and quantify the access of the electrolyte to the Pt active sites. Figure 4 presents the activation cycles for the three carbon-capped catalysts. For the sake of comparison, a similar activation protocol was also applied on the commercial materials Pt/Gr.C and PtNi/VC, despite no specific activation is expected on these uncapped materials, except the electrochemical evolution and aging of the nanoparticles due to repeated cycles at high potential. Figure 4 A to E present the last (200^{th}) cycles for each UPL at a scan rate of 500 mV s^{-1}; the (CVs) at 20 mV s^{-1} (Figure 4 F to J) were recorded to obtain well-defined curves to measure the H_{upd}. In the present case, the carbon cap totally prevents the electrolyte from accessing the Pt sites initially, as it can be seen on the first CV. Then, the controlled and stepwise activation of the carbon-capped catalysts is obtained as the Upper Limit Potential gets higher and higher, favoring the partial oxidation of the carbon-cap (into CO_2).

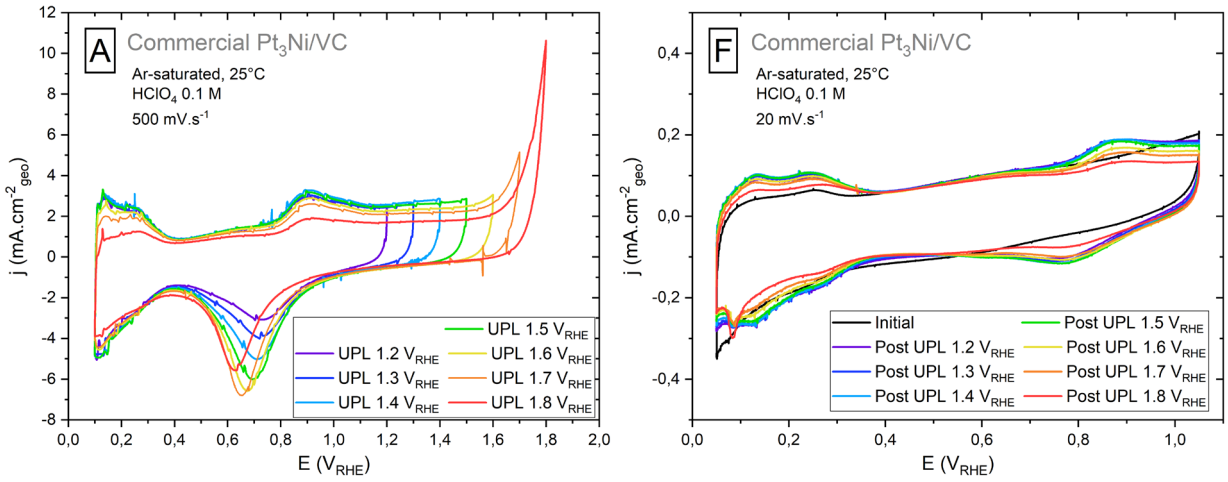

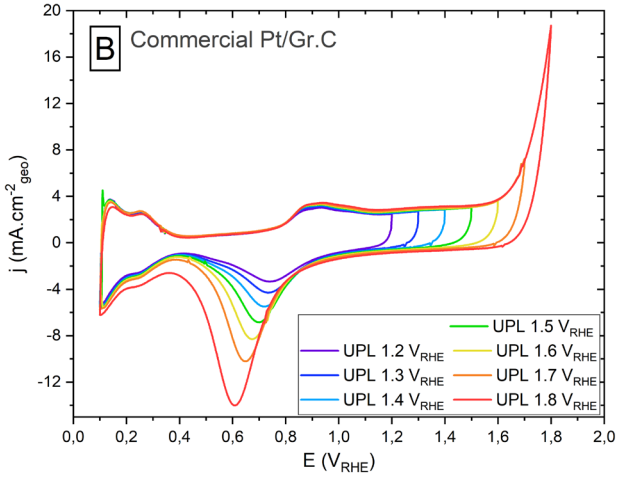
B
Commercial Pt/Gr.C
j (mA.cm-2geo)
E (VRHE)
UPL 1.5 VRHE
UPL 1.2 VRHE
UPL 1.6 VRHE
UPL 1.3 VRHE
UPL 1.7 VRHE
UPL 1.4 VRHE
UPL 1.8 VRHE

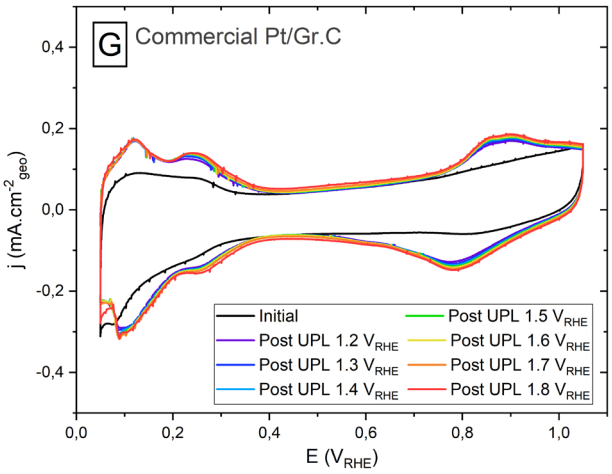
G
Commercial Pt/Gr.C
j (mA.cm-2geo)
E (VRHE)
Initial
Post UPL 1.5 VRHE
Post UPL 1.2 VRHE
Post UPL 1.6 VRHE
Post UPL 1.3 VRHE
Post UPL 1.7 VRHE
Post UPL 1.4 VRHE
Post UPL 1.8 VRHE

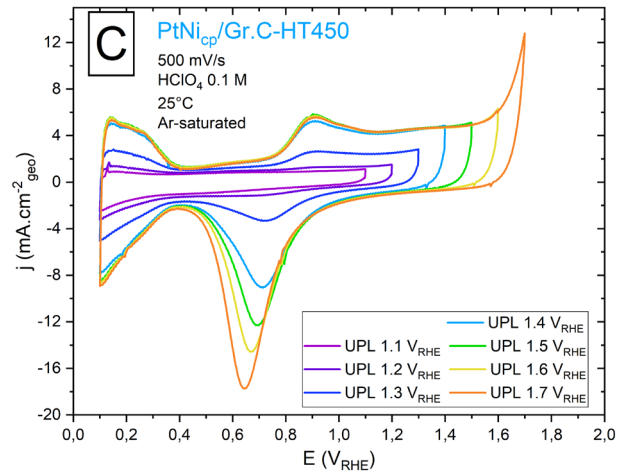
C
PtNicp/Gr.C-HT450
500 mV/s
HClO4 0.1 M
25°C
Ar-saturated
j (mA.cm-2geo)
E (VRHE)
UPL 1.4 VRHE
UPL 1.1 VRHE
UPL 1.5 VRHE
UPL 1.2 VRHE
UPL 1.6 VRHE
UPL 1.3 VRHE
UPL 1.7 VRHE

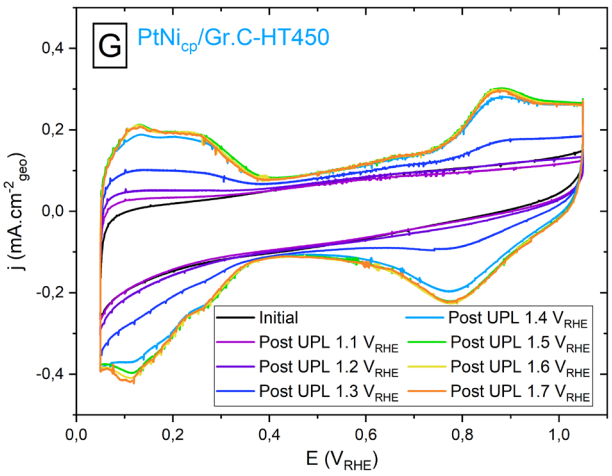
G
PtNicp/Gr.C-HT450
j (mA.cm-2geo)
E (VRHE)
Initial
Post UPL 1.4 VRHE
Post UPL 1.1 VRHE
Post UPL 1.5 VRHE
Post UPL 1.2 VRHE
Post UPL 1.6 VRHE
Post UPL 1.3 VRHE
Post UPL 1.7 VRHE

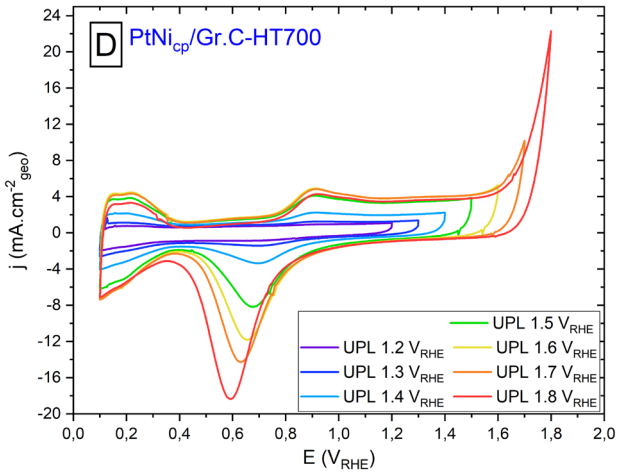
D
PtNicp/Gr.C-HT700
j (mA.cm-2geo)
E (VRHE)
UPL 1.5 VRHE
UPL 1.2 VRHE
UPL 1.6 VRHE
UPL 1.3 VRHE
UPL 1.7 VRHE
UPL 1.4 VRHE
UPL 1.8 VRHE

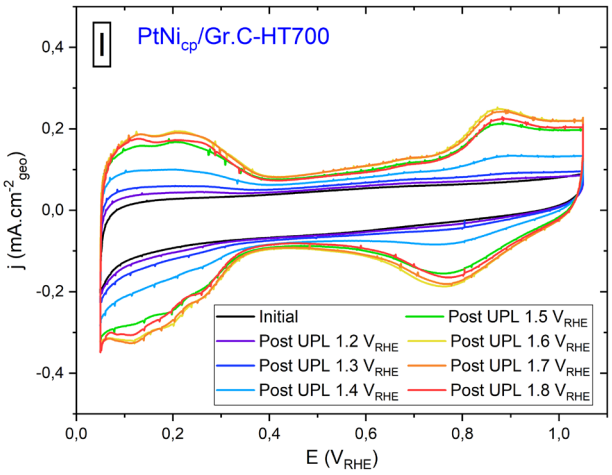
I
PtNicp/Gr.C-HT700
j (mA.cm-2geo)
E (VRHE)
Initial
Post UPL 1.5 VRHE
Post UPL 1.2 VRHE
Post UPL 1.6 VRHE
Post UPL 1.3 VRHE
Post UPL 1.7 VRHE
Post UPL 1.4 VRHE
Post UPL 1.8 VRHE

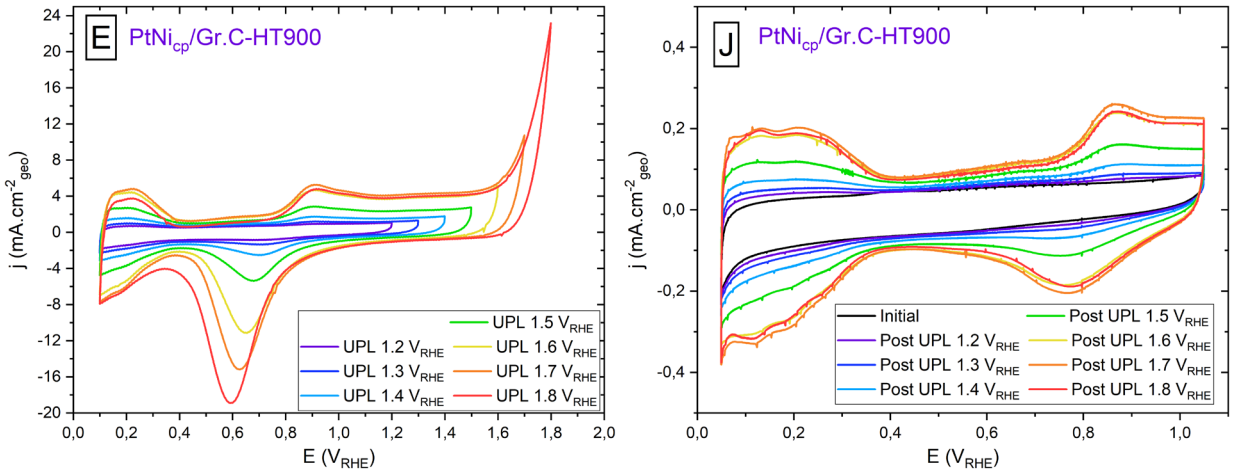

Figure 4: First activation procedure: (A-E) 200th CV curves for each UPL activation steps recorded at 500 mV s^{-1} and (F-J) corresponding intermediate CV curves for each UPL activation steps recorded at 20 mV s^{-1} for all carbon-capped PtNi/Gr.C electrocatalysts. Electrolyte Ar-saturated $HClO_4$ 0.1 M, 25°C.

The CVs show clear fingerprint features of H_{upd} at Pt surfaces (0.05−0.4 V *vs* RHE), Electric Double-Layer (EDL) region (0.4−0.7 V *vs* RHE), and Pt oxidation/reduction (above 0.7 V *vs* RHE). The activation CVs, recorded at high scan rate, show an increase and shift of the platinum-oxides reduction peaks as the UPL increases, due to the kinetically irreversible place-exchange process and the increased Pt-oxides coverage with UPL [41]. For the highest UPL activation steps, oxygen evolution currents are observed and additional argon purging time between those UPL steps was applied to ensure Ar-saturated electrolyte before intermediate CVs. Overall, for the two commercial catalysts, without any carbon-cap, an increase of the H_{upd} coulometry is noticed after the first set of activation cycles and reaches a maximum after the first UPL step (in fact few tens of cycles were enough); this is due to the desorption of pristine-organic contamination of Pt sites [42]. While the Pt/Gr.C voltamogramm is rather stable post cycles at UPL 1.2 V *vs* RHE, its H_{upd} coulometry remains constant throughout the whole procedure. In contrast, the Pt_3Ni/VC show a decrease in H_{upd} signal above UPL 1.5 V *vs* RHE. This is probably related to the less robust Vulcan carbon support than the graphitic carbon support, which promotes (after oxidation) detachment of PtNi NPs.

For the carbon-capped catalysts, the H_{upd} coulometry increases progressively as the UPL rises. Ji *et al.* [24], who performed similar activation procedure, suggested through differential electrochemical mass spectrometry (DEMS) studies that the carbon-cap is partially oxidized into CO_2, catalyzed by the Pt [43]. This process forms a porous cap, that leaves the reactant access Pt sites. The three carbon-capped catalysts also show a slight increase of their EDL, which can be attributed to the progressive unleashing of the Pt EDL contribution, initially hindered before activation. Finally, the carbon-capped catalysts turn out to be fully activated after UPL 1.4/1.5, 1.5/1.6 and 1.6 V *vs* RHE at 450, 700 and 900°C, respectively, showing that the higher the heat-treatment temperature, the more robust the carbon-cap against electrochemical corrosion (and the harsher the activation procedure required).

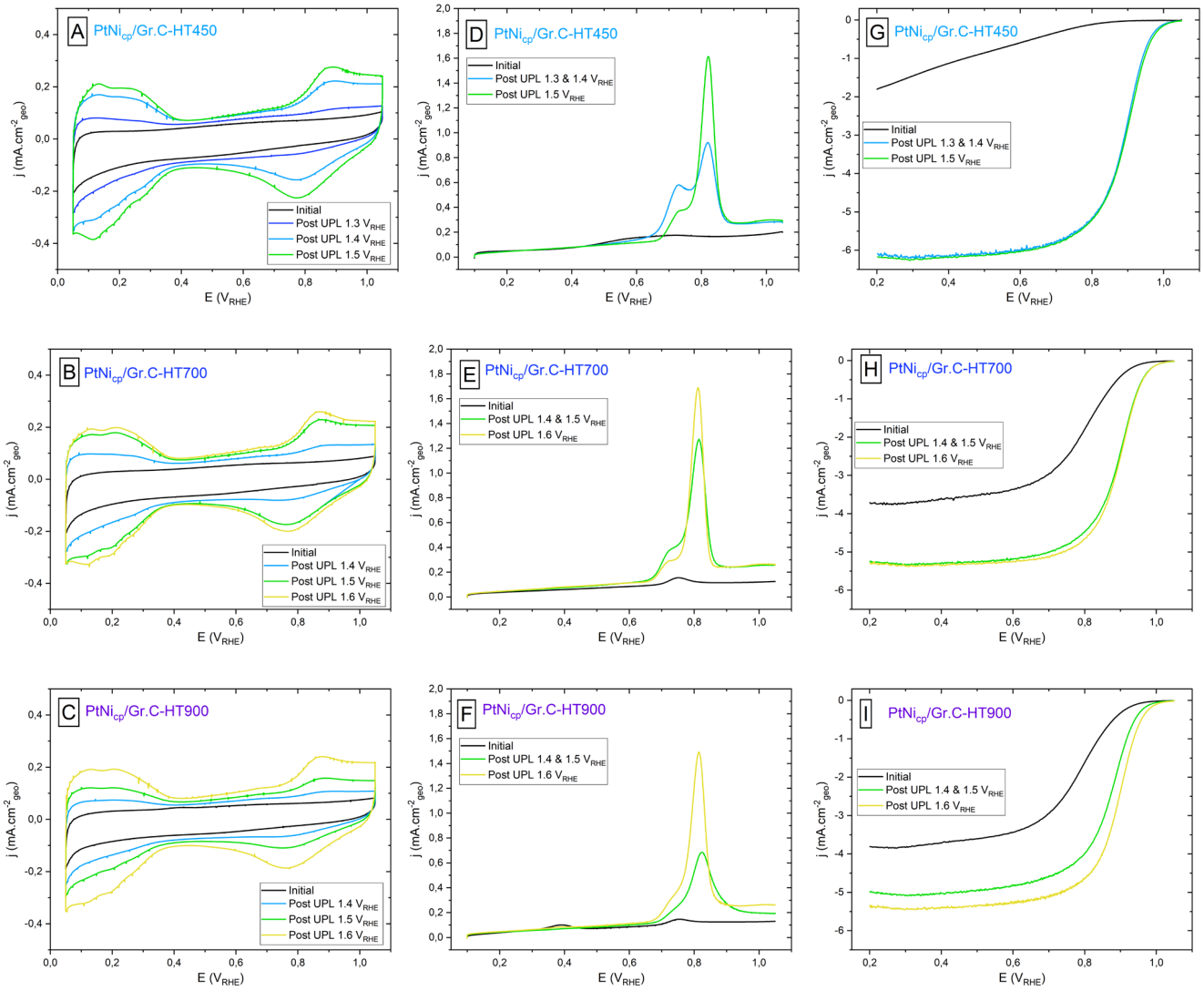

<u>Figure 5:</u> Evolution of the respective voltammograms for the three carbon-capped PtNi/Gr.C electrocatalysts during the activation protocols: (A, B, C) 20 mV s^{-1} in Ar-saturated 0.1 M $HClO_4$; (D, E, F) 20 mV s^{-1} positive scan for CO-stripping; (G, H, I) 20 mV s^{-1} positive scan for ORR measurement in O_2-saturated electrolyte at 1600 rpm.

Once the UPL to fully activate the three carbon-capped PtNi/Gr.C electrocatalysts is known, another experiment (with a new dropcast from the same ink) is performed to measure their ECSA and ORR catalytic activity. For the activation, three UPL steps (three sets of 200 cycles) are performed to ensure activation similar to the previous experiment, and they allow intermediate characterizations. Figure 5 A-C gathers the CV at 20 mV.s^{-1} recorded prior and after each UPL activation step and Figure 5 D-I represents CO-stripping and ORR polarization curves performed at the initial state, after the two firsts UPL activation steps and after the third one.

As expected, at the initial state, the catalysts exhibit almost no specific CO adsorption and very poor ORR activity, due to the blocking of the Pt sites by the carbon cap. In the CO-stripping curves, two peaks are observed: the dominant one is measured at *ca*. 0.8 V *vs* RHE; it is characteristic of the oxidation of CO onto polycrystalline Pt

surfaces, as described in previous studies [44]. For all the catalysts, a pre-peak is observed at *ca*. 0.7 V *vs* RHE, that could be ascribed to the presence of agglomerated NPs and consequent grain boundaries, where the CO can be easily oxidized [44]. However, the intermediate CO-stripping voltamograms after 3 UPL activation steps show that the pre-peak decreases in intensity, suggesting that it might not be related to the grain boundaries, because there is no NPs agglomeration/sintering during the activation step. Indeed, this multiple-peak voltammogram can also be related to the existence of surfaces with step defects: "step sites are less active to oxidize CO than those ones responsible for the CO pre-oxidation process" [45]. In addition, the progressive activation of the NPs might give rise to an increase in surface defects, especially due to the progressive leaching of Ni atoms. The latter trend (decrease of the pre-peak) can be due to a subsequent smoothening (electrochemical annealing of these defects [46]) or, *via* a change in lattice parameter, shift the onset potential of the pre-peak, but this was not observed here [47].

After the optimal activation in terms of Pt active surface area and ORR activity, the state of the carbon-cap can be questioned. Figure S3 displays a TEM image of the $PtNi_{cp}$/Gr.C-HT900 post activation, showing that the carbon-cap is still present. Nevertheless, the porosity of the cap is not noticeable, due to the small size and awkward contrast (the carbon-capped NPs are supported on a carbon support). EDS analysis conducted on large aggregates suggest a Pt:Ni atomic composition close to 3:1 after activation, corroborating the leaching of Ni atoms during the activation procedure also witnessed in XRD.

The protocol was reproduced three times for each catalyst to obtain mean values of the maximum active surface area and intrinsic activity for ORR, which are reported in the Table 1. ECSA were evaluated by CO-stripping and H_{upd}, the latter known to underestimate the real ECSA, because of incomplete coverage of H_{ads} on Pt sites between 0.05 and 0.4 V *vs* RHE, even more for bimetallic catalysts [48]. The carbon-capped catalysts exhibit mass activities (MA) superior to the mother Pt/Gr.C catalyst, probably due to ligand and strain effects coming from the incorporation of Ni in the Pt lattice [40]. The activities also match those of the un-capped commercial Pt_3Ni/VC catalyst, denoting for the negligible hindrance of the carbon-cap regarding the ORR and the access of reactants (O_2 and H^+). It is noteworthy that ECSAs measured by CO-stripping are higher for the carbon-capped catalysts than for the two benchmarks, despite larger average particle size. It is suggested that higher ECSA originates from the activation steps that, by potential cycling, leaches-out surface Ni atom and creates a porous Pt outer-layer (Pt-skeleton) with abundant defects and further increased ECSA. This behavior could also come from hydrogen/carbon monoxide spillover, as suggest by Karuppannan *et al*. [49], but asserting this would require further investigation.

These characterizations demonstrate that, whatever the degree of graphitization of their initial carbon-cap, the carbon-capped catalysts can all be (rather easily) activated electrochemically, leading to similar ECSA and ORR activities. Hence, these materials may have some interest for use at the cathode of a PEMFC, provided their durability is satisfactory, which will be tested in the next section.

Table 1: ORR Mass activities (MA) calculated at 0.9 V vs RHE, ECSA determined by CO-stripping and Hupd, and ORR Specific activities (SA).

Catalyst materials	**ECSA (m^2/g_{Pt}) (CO-stripping)**	**ECSA (m^2/g_{Pt}) (Hupd)**	**MA (A/g_{Pt})**	**SA ($\mu A/cm^2_{Pt}$) (CO-stripping)**
Commercial Pt/Gr.C	35 ± 3	18 ± 2	171 ± 15	489
Commercial Pt_3Ni/VC	38 ± 2	26 ± 2	209 ± 26	550
PtNicp/Gr.C-HT450	50 ± 2	37 ± 2	207 ± 36	414
PtNicp/Gr.C-HT700	50 ± 1	34 ± 1	218 ± 15	436
PtNicp/Gr.C-HT900	51 ± 1	33 ± 4	228 ± 15	447

3.3. Durability assessment

The Accelerated Stress Test (AST) used herein is derived from FCCJ (Fuel Cell Commercialization Conference of Japan) recommendations[50] for base-load operation, *i.e.* square waves cycles with potential holding of 3 s at the UPL and Lower Potential Limit (LPL). The main difference with the original AST lies in the temperature of the cell during the AST; instead of room temperature (which is too mild of an AST for this class of catalysts [23]: the two benchmarks are rather stable during AST at 25°C), the temperature was increased to 80°C, to accelerate the degradation rates and be closer to real PEMFC operation [51].

Figure 6-A presents the different phases of the aging protocol used in this study. Firstly, the respective and optimal activation procedure has been applied for each carbon-capped catalysts, as described previously, using the most suitable UPL value prior to the first characterization block. This step makes it possible to evaluate the actual protective effect of the activated carbon-cap in fair comparison with the benchmark catalysts, by monitoring the trend related to ECSA/MA retention. Indeed, many studies show a better durability of carbon-capped catalysts, but as the catalysts are mostly not fully activated before aging, the enhanced durability might come from an artificial delay with inactive material at the beginning of test (the time to activated the carbon cap). Let it be stressed also that the benchmarks catalysts were cycled at 500 mV s^{-1} between 0.05 and 1.2 V *vs* RHE (50 cycles – this is by no means as intensive as the activation step for the carbon-capped catalysts) to remove contamination until stabilization prior to the initial characterization phase.

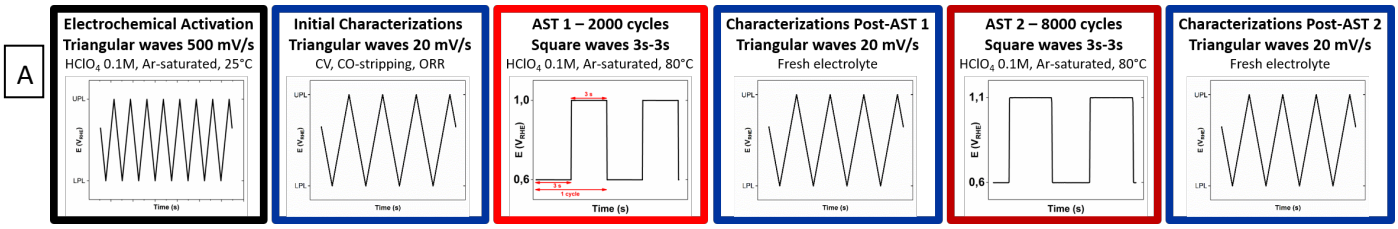

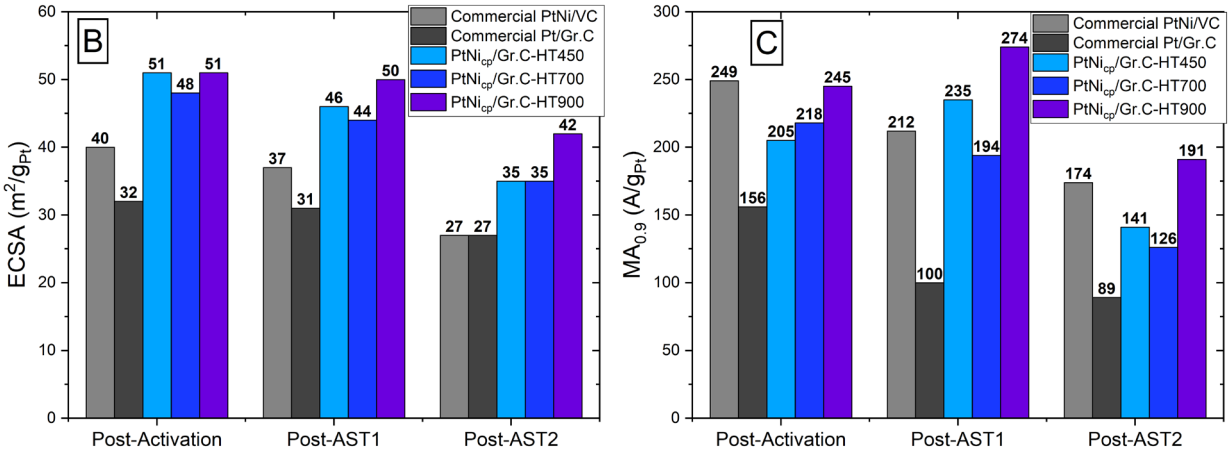

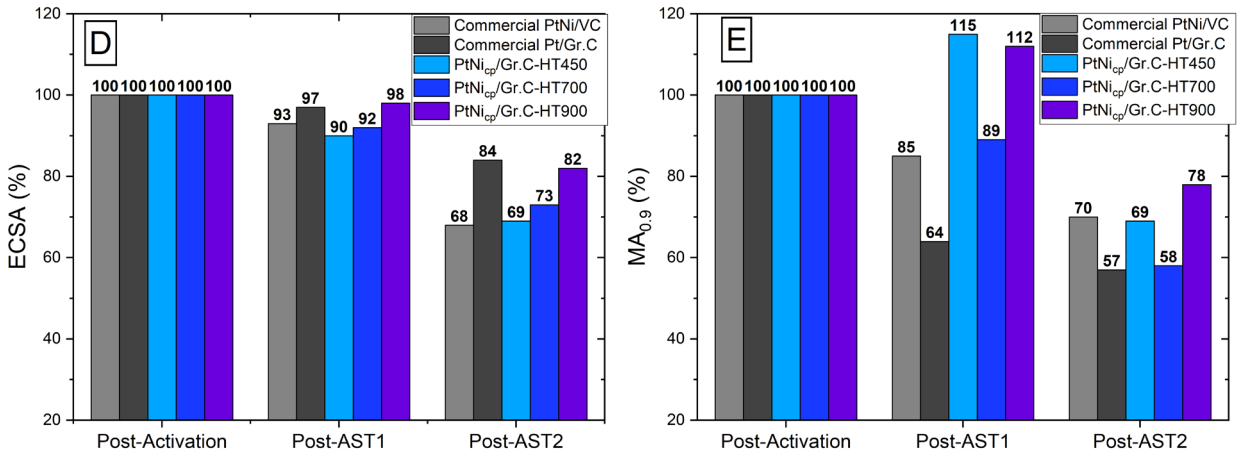

Figure 6: (A) Description of AST protocol (B) ECSA measured by CO-stripping and (C) mass activities measured at 0.9 V vs RHE during the characterization phases after activation and after each AST block, for all the catalysts tested herein.

The aging protocol, performed at 80°C to be sufficiently severe to degrade this class of catalysts, is then divided into two parts: a first AST block (AST1) consists of 2000 cycles (6 s each) between 0.6 and 1.0 V *vs* RHE to focus on Oswald ripening and dissolution-redeposition degradations. The second AST block (AST2) is composed of 8000 cycles between 0.6 and 1.1 V *vs* RHE, to increase even more the degradation rate (favoring the place-exchange mechanism of the Pt-based NPs and accelerating the rate of Pt and Ni dissolution). Here, it must be noted that the higher potential limit was not elevated more, not to promote significant carbon corrosion that could happen in start and stop events (which was beyond the scope of the present study). Electrochemical characterizations (CO-stripping, pseudo-ORR (pORR) to correct for the double layer current, and ORR) are also performed after both AST blocks. After each AST phase, the electrolyte is changed and the cell is cleaned with DI water to avoid any reversible degradation [23] (due to possible electrolyte decomposition, Pt^{2+} and Ni^{2+} contamination following their possible leaching during the AST, reversible oxide formation). The intermediate AST allows to assure, by decreased ECSA, that the thin film was fully wetted and that the carbon-capped catalysts are fully activated, preventing delayed degradation by carbon sacrificial oxidation.

The two benchmark catalysts, having similar particles sizes but different carbon support and different NPs composition, exhibit the same degradation behavior: their final ECSA is identical (27 $m^2.g_{Pt}^{-1}$) and the PSD evolution after AST is similar (around 20% mean particle size increase, Figure 7). This result suggests that the carbon support corrosion is not major during our AST, as intended by the conditions chosen. The commercial Pt_3Ni/VC maintains rather good ORR activity after the AST (loss of 15% of MA), suggesting a (partial) retention of Ni in these conditions. However, its textural properties changed significantly, with non-negligible nanoparticles size growth (Figure 7), that scales with the ECSA loss (Figure 6); it is therefore possible that the deleterious effect of the active area loss (and possibly loss of Ni from the mother alloy) is partly counterbalanced by an increase of the intrinsic activity, owing to the classical positive particle size effect for ORR catalysis [52,53]. The Pt/Gr.C has a near-similar behavior; it losses ca. 36% in MA after the first AST, which can essentially be ascribed to the non-negligible nanoparticles size growth (Figure 7): Pt dissolution-redeposition onto larger particle can be deduced from the PSDs, as the number of small NPs decrease at the profit of larger ones, and this NPs growth is the main reason for the MA loss.

After the AST1, Figure 6 shows a clear protective effect of the carbon cap in terms of electrochemical properties (ECSA and MA retention). The increase of the mass activities of the carbon-capped catalysts elaborated at 450 and 900°C of heat-treatment after AST may come from a non-fully complete activation of the capped catalyst after the activation step. However, and since the ECSA decreased after AST1 (which contradicts the previous statement), it is rather believed that this behavior could be ascribed to a surface restructuring occurring during the AST1 ; it could be linked to the (partial) leaching of surface Ni, leading to a so-called Pt skeleton structure, that is known to enhance MA [54]. The trend after AST2 (a much more aggressive AST) is less clear in terms of electrochemical properties (even though, structurally, the carbon-capped catalysts are obviously more stable than their uncapped counterparts – Figure 7): the carbon-capped catalysts showed 31%, 27% and 18% ECSA losses for synthesis temperatures of 450, 700 and 900°C, respectively. In comparison of the 33 and 16% ECSA loss of PtNi/VC and Pt/Gr.C benchmarks, there is no clear evidence of the carbon-cap on Pt dissolution, taking the ECSA loss as an indicator. However, one can observe a trend regarding the degree of graphitization of the carbon-cap. The more resistant carbon-capped catalyst (900°C) seems able to better withstand the AST (in particular the second block - AST2 - with UPL at 1.1 V *vs* RHE) and its influence lasts longer; this trend is confirmed by the PSD analysis of the TEM micrographs (Figure 7): while the benchmarks show a 20% PSD increase, carbon-capped catalysts treated at 450, 700 and 900°C have their PSD increase by only 10, 5 and 3%, respectively. One could argue that the mean NP sizes are slightly bigger initially for the carbon-capped catalysts than for the benchmarks; however, this does not seem to be the explanation; indeed, the three carbon-capped catalysts have near-similar initial mean particle size, so the observed trend is likely linked to the structure of the carbon-cap. In terms of MA, the carbon-capped catalysts show much smaller ORR kinetic losses than the benchmarks after AST1, revealing a positive effect of the carbon cap. AST2, on the contrary, seems too aggressive to the carbon (cap and perhaps support) of the two catalysts elaborated at 450 and 700°C; only the one heat-treated at 900°C really seems to maintain an advantage over the two benchmark catalysts after AST2.

One could argue that the commercial Pt_3Ni/VC catalyst has a much more amorphous carbon support than the graphitized carbon black of the carbon-capped catalysts, which should be more prone to carbon corrosion. However, the two AST used were essentially designed to test the robustness of the Pt(Ni) nanoparticles, and not those of the carbon support, which is essentially demonstrated by the TEM data of Figure 7 (this is the reason why 1.1 V *vs* RHE was the highest upper potential limit applied in the ASTs). So in essence, carbon corrosion is not the primary mode of degradation in the present conditions, and the authors believe it is still relevant to compare the fate of the carbon-capped PtNi/Gr.C and uncapped PtNi/VC materials (in these conditions).

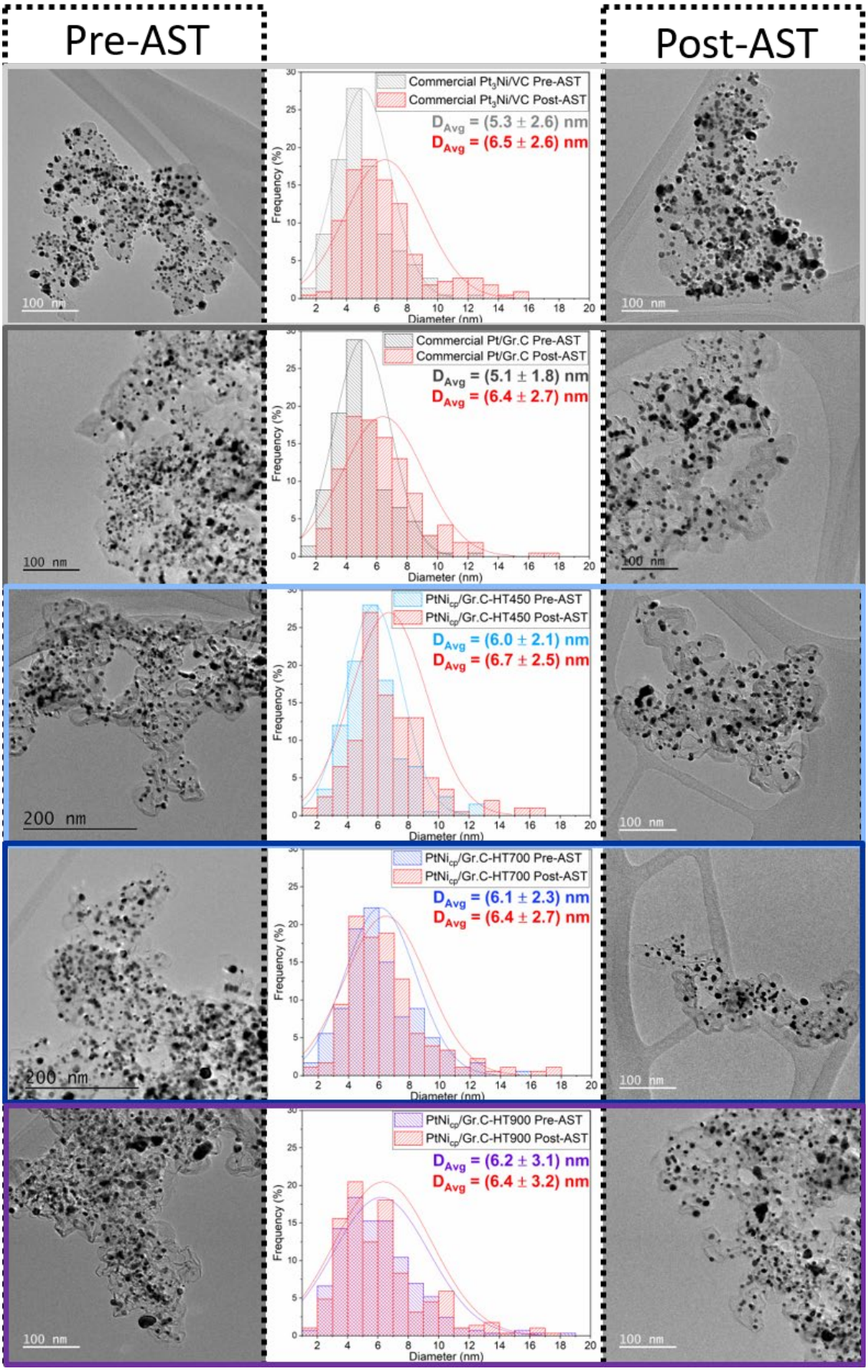
Pre-AST
Post-AST
Commercial Pt3Ni/VC Pre-AST
Commercial Pt3Ni/VC Post-AST
DAvg = (5.3 ± 2.6) nm
DAvg = (6.5 ± 2.6) nm
Commercial Pt/Gr.C Pre-AST
Commercial Pt/Gr.C Post-AST
DAvg = (5.1 ± 1.8) nm
DAvg = (6.4 ± 2.7) nm
PtNicp/Gr.C-HT450 Pre-AST
PtNicp/Gr.C-HT450 Post-AST
DAvg = (6.0 ± 2.1) nm
DAvg = (6.7 ± 2.5) nm
PtNicp/Gr.C-HT700 Pre-AST
PtNicp/Gr.C-HT700 Post-AST
DAvg = (6.1 ± 2.3) nm
DAvg = (6.4 ± 2.7) nm
PtNicp/Gr.C-HT900 Pre-AST
PtNicp/Gr.C-HT900 Post-AST
DAvg = (6.2 ± 3.1) nm
DAvg = (6.4 ± 3.2) nm
Frequency (%)
Diameter (nm)
100 nm
200 nm

Figure 7: TEM images before and after the AST, and PSD associated.

4. Conclusion

Carbon-capped PtNi catalysts were prepared from a mother commercial Pt/Gr.C catalyst and a nickel organometallic compound (bis(cyclopentadienyl)Ni(II)). The dry mixture and appropriate heat-treatment of this organometallic precursor with this conventional Pt/Gr.C catalyst can lead to carbon-capped PtNi alloy catalysts, that can be tuned in terms of degree of alloying of the PtNi core and of graphitization/organization of the carbon cap. A proper electrochemical activation procedure further enables to reveal the maximum activity of the carbon-capped PtNi catalysts, for any degree of graphitization of the carbon cap. This procedure allows a more reliable durability assessment of the carbon-capped catalysts, as it rules out the sacrificial role of the carbon cap during activation. The results of the conventional base-load AST (AST1: 0.6-1 V *vs* RHE, 80°C, 2000 cycles) show rather significant durability improvement of the carbon-capped catalysts compared to the two commercial benchmark catalysts (Pt/Gr.C and Pt_3Ni/VC), but the benefit of the carbon cap essentially levels off for the (significantly more) aggressive AST2 (0.6 – 1.1 V *vs* RHE, 80°C, 8000 cycles), at least for the two carbon-capped catalysts heat-treated at 450 and 700°C. Nevertheless, the catalyst heat-treated at 900°C seems slightly more robust in these conditions, even than the Pt/Gr.C material, which is a true benchmark in terms of robustness towards harsh operating conditions that are desired for heavy-duty PEMFCs.

In terms of catalysts' textural properties, *post mortem* TEM micrographs and related PSD histograms show a clear trend in particle size/morphology retention with the degree of graphitization of the carbon cap. More in-depth studies like EC-ICP-MS online have to be performed to unveil a possible benefit of the carbon-capped catalysts towards Pt dissolution. In any case, one should always use a highly-graphitized carbon cap to avoid its decomposition during harsh operating conditions (*e.g*. AST) and in general in real PEMFC system for the cathode; such graphitization requires a high temperature heat-treatment and a rather severe activation procedure. In that case, the influence of the heat-treatment of the NPs and carbon support have to be considered.

In summary, if the carbon cap is properly graphitized and activated, it can result in high electrochemical activity (higher than uncapped commercial benchmarks) which can be maintained over longer test durations/harsher AST than for uncapped catalysts. It must be noted, though, that while the electrochemical activation can be a powerful tool to monitor and evaluate carbon-capped catalysts, it cannot be applied in real PEMFC system; this will require an *ex situ* activation protocol, which is presently evaluated in our teams.

Supporting Information

TGA profile, more TEM micrographs and additional electrochemical results are provided in supporting information.

Acknowledgements

QL's PhD thesis is part of the PEMFC95 project, funded by France's "Programme d'Investissements d'Avenir" operated by the French National Research Agency (grant ANR-22-PEHY-0005). Some of this work has been performed within the framework of the Centre of Excellence of Multifunctional Architectured Materials "CEMAM", Grenoble France n◦ ANR-10-LABX-44–01. The authors also kindly thank Marta Mirolo from the European Synchrotron Radiation Facility (ESRF) for the acquisition of XRD diffractograms, and Vincent Martin from LEPMI for the ICP-MS measurements used for the determination of the Pt on carbon loadings.

Conflict of Interest

The authors have no conflict of interest to declare.

References

[1] Cullen DA, Neyerlin KC, Ahluwalia RK, Mukundan R, More KL, Borup RL, et al. New roads and challenges for fuel cells in heavy-duty transportation. Nat Energy 2021;6:462–74. https://doi.org/10.1038/s41560-021-00775-z.

[2] Dubau L, Castanheira L, Maillard F, Chatenet M, Lottin O, Maranzana G, et al. A review of PEM fuel cell durability: materials degradation, local heterogeneities of aging and possible mitigation strategies. WIREs Energy Environ 2014;3:540–60. https://doi.org/10.1002/wene.113.

[3] Cherevko S, Kulyk N, Mayrhofer KJJ. Durability of platinum-based fuel cell electrocatalysts: Dissolution of bulk and nanoscale platinum. Nano Energy 2016;29:275–98. https://doi.org/10.1016/j.nanoen.2016.03.005.

[4] Wang G, Yu Y, Liu H, Gong C, Wen S, Wang X, et al. Progress on design and development of polymer electrolyte membrane fuel cell systems for vehicle applications: A review. Fuel Process Technol 2018;179:203–28. https://doi.org/10.1016/j.fuproc.2018.06.013.

[5] Parthasarathy P, Virkar AV. Electrochemical Ostwald ripening of Pt and Ag catalysts supported on carbon. J Power Sources 2013;234:82–90. https://doi.org/10.1016/j.jpowsour.2013.01.115.

[6] Tang L, Han B, Persson K, Friesen C, He T, Sieradzki K, et al. Electrochemical Stability of Nanometer-Scale Pt Particles in Acidic Environments. J Am Chem Soc 2010;132:596–600. https://doi.org/10.1021/ja9071496.

[7] Yano H, Watanabe M, Iiyama A, Uchida H. Particle-size effect of Pt cathode catalysts on durability in fuel cells. Nano Energy 2016;29:323–33. https://doi.org/10.1016/j.nanoen.2016.02.016.

[8] Robledo Candia LD, Lavorato GC, Rubert AA, Fonticelli MH. Electrochemical stability of metal nanoparticles: The role of size-distribution broadness. Electrochimica Acta 2024;475:143546. https://doi.org/10.1016/j.electacta.2023.143546.

[9] Antolini E. Alloy vs. intermetallic compounds: Effect of the ordering on the electrocatalytic activity for oxygen reduction and the stability of low temperature fuel cell catalysts. Appl Catal B Environ 2017;217:201–13. https://doi.org/10.1016/j.apcatb.2017.05.081.

[10] Chougule SS, Jeffery AA, Roy Chowdhury S, Min J, Kim Y, Ko K, et al. Antipoisoning catalysts for the selective oxygen reduction reaction at the interface between metal nanoparticles and the electrolyte. Carbon Energy 2023;5:e293. https://doi.org/10.1002/cey2.293.

[11] Chen S, Wei Z, Qi X, Dong L, Guo Y-G, Wan L, et al. Nanostructured Polyaniline-Decorated Pt/C@PANI Core–Shell Catalyst with Enhanced Durability and Activity. J Am Chem Soc 2012;134:13252–5. https://doi.org/10.1021/ja306501x.

[12] Daimon H, Yamazaki S, Asahi M, Ioroi T, Inaba M. A Strategy for Drastic Improvement in the Durability of Pt/C and PtCo/C Alloy Catalysts for the Oxygen Reduction Reaction by Melamine Surface Modification. ACS Catal 2022;12:8976–85. https://doi.org/10.1021/acscatal.2c01942.

[13] Hu Y, Zhang J, Shen T, Lu Y, Chen K, Tu Z, et al. A Low-Temperature Carbon Encapsulation Strategy for Stable and Poisoning-Tolerant Electrocatalysts. Small Methods 2021;5:2100937. https://doi.org/10.1002/smtd.202100937.

[14] Kim Y, Jang J-H, Min J, Jeffery AA, Lee S, Chougule SS, et al. A target-customized carbon shell structure of carbon-encapsulated metal nanoparticles for fuel cell applications. J Mater Chem A 2021;9:24480–7. https://doi.org/10.1039/D1TA06289A.

[15] Lee D, Kim Y, Song J, Choi HJ, Karuppannan M, Cho Y-H, et al. Variations in Electrochemical Characteristics of a Platinum Catalyst Enwrapped by a Carbon Shell According to Carbon Layer Thickness. ACS Appl Energy Mater 2022;5:596–603. https://doi.org/10.1021/acsaem.1c03098.

[16] Li Z, Zou J, Xi X, Fan P, Zhang Y, Peng Y, et al. Native Ligand Carbonization Renders Common Platinum Nanoparticles Highly Durable for Electrocatalytic Oxygen Reduction: Annealing Temperature Matters. Adv Mater 2022;34:2202743. https://doi.org/10.1002/adma.202202743.

[17] Yamada H, Kato H, Kodama K. Cell Performance and Durability of Pt/C Cathode Catalyst Covered by Dopamine Derived Carbon Thin Layer for Polymer Electrolyte Fuel Cells. J Electrochem Soc 2020;167:084508. https://doi.org/10.1149/1945-7111/ab8b97.

[18] Yan Z, Zhang Y, Dai C, Zhang Z, Zhang M, Wei W, et al. Porous, thick nitrogen-doped carbon encapsulated large PtNi core-shell nanoparticles for oxygen reduction reaction with extreme stability and activity. Carbon 2022;186:36–45. https://doi.org/10.1016/j.carbon.2021.10.004.

[19] Tong X, Zhang J, Zhang G, Wei Q, Chenitz R, Claverie JP, et al. Ultrathin Carbon-Coated Pt/Carbon Nanotubes: A Highly Durable Electrocatalyst for Oxygen Reduction. Chem Mater 2017;29:9579–87. https://doi.org/10.1021/acs.chemmater.7b04221.

[20] Dai Y, Di S, Guo Y, Wang F, Wang Z, Zhu H. Carbon layers derived from zeolitic imidazolate framework crystal shells as a protective layer for Pt-based catalysts: Boosting oxygen reduction catalytic activity in fuel cells. Int J Hydrog Energy 2024;57:1457–65. https://doi.org/10.1016/j.ijhydene.2024.01.050.

[21] Jiang Y, Wang Y, Qian J, Mu Y, Li Z, Zhao T, et al. Durable carbon-shell-encapsulated Pt/C catalysts synthesized by direct pyrolysis of Pt-pyrrole complexes for the oxygen reduction reaction. Int J Hydrog Energy 2024;51:578–86. https://doi.org/10.1016/j.ijhydene.2023.06.328.

[22] Liu Q, Ranocchiari M, Van Bokhoven JA. Catalyst overcoating engineering towards high-performance electrocatalysis. Chem Soc Rev 2022;51:188–236. https://doi.org/10.1039/D1CS00270H.

[23] Dubau L, Maillard F. Unveiling the crucial role of temperature on the stability of oxygen reduction reaction electrocatalysts. Electrochem Commun 2016;63:65–9. https://doi.org/10.1016/j.elecom.2015.12.011.

[24] Ji SG, Kwon HC, Kim T-H, Sim U, Choi CH. Does the Encapsulation Strategy of Pt Nanoparticles with Carbon Layers Really Ensure Both Highly Active and Durable Electrocatalysis in Fuel Cells? ACS Catal 2022;12:7317–25. https://doi.org/10.1021/acscatal.2c01618.

[25] Guo L, Jiang W-J, Zhang Y, Hu J-S, Wei Z-D, Wan L-J. Embedding Pt Nanocrystals in N-Doped Porous Carbon/Carbon Nanotubes toward Highly Stable Electrocatalysts for the Oxygen Reduction Reaction. ACS Catal 2015;5:2903–9. https://doi.org/10.1021/acscatal.5b00117.

[26] Sgarbi R, Doan H, Martin V, Chatenet M. Tailoring the Durability of Carbon-Coated Pd Catalysts Towards Hydrogen Oxidation Reaction (HOR) in Alkaline Media. Electrocatalysis 2023;14:267–78. https://doi.org/10.1007/s12678-022-00794-8.

[27] Doan H, Sgarbi R, Labarde Q, Martin V, Chatenet M. One-Pot Synthesis of Carbon-Supported Pd Nanoparticles with Ni and Carbon Matrix Protection for Durable Alkaline Hydrogen Oxidation Reaction. ChemCatChem 2024:e202400154. https://doi.org/10.1002/cctc.202400154.

[28] Doan H, Sgarbi R, Labarde Q, Martin V, Chatenet M. One-pot Synthesis of Carbon-supported Pd Nanoparticles with Ni and Carbon Matrix Protection for Durable Alkaline Hydrogen Oxidation Reaction. ChemCatChem n.d.

[29] Zhu S, Hu X, Zhang L, Shao M. Impacts of Perchloric Acid, Nafion, and Alkali Metal Ions on Oxygen Reduction Reaction Kinetics in Acidic and Alkaline Solutions. J Phys Chem C 2016;120:27452–61. https://doi.org/10.1021/acs.jpcc.6b09769.

[30] Garsany Y, Singer IL, Swider-Lyons KE. Impact of film drying procedures on RDE characterization of Pt/VC electrocatalysts. J Electroanal Chem 2011;662:396–406. https://doi.org/10.1016/j.jelechem.2011.09.016.

[31] Zheng W. *iR* Compensation for Electrocatalysis Studies: Considerations and Recommendations. ACS Energy Lett 2023;8:1952–8. https://doi.org/10.1021/acsenergylett.3c00366.

[32] Pugmire DL, Woodbridge CM, Boag NM, Langell MA. Adsorption and decomposition of nickelocene on Ag(100): a high-resolution electron energy loss spectroscopy and temperature programmed desorption study. Surf Sci 2001;472:155–71. https://doi.org/10.1016/S0039-6028(00)00939-0.

[33] Avery NR. Adsorption and reactivity of 1-3 cyclopentadiene on Pt(111). J Electron Spectrosc Relat Phenom 1986;39:1–9. https://doi.org/10.1016/0368-2048(86)85026-5.

[34] Popov AA, Varygin AD, Plyusnin PE, Sharafutdinov MR, Korenev SV, Serkova AN, et al. X-ray diffraction reinvestigation of the Ni-Pt phase diagram. J Alloys Compd 2022;891:161974. https://doi.org/10.1016/j.jallcom.2021.161974.

[35] Tulić S, Waitz T, Čaplovičová M, Habler G, Vretenár V, Susi T, et al. Catalytic graphitization of single-crystal diamond. Carbon 2021;185:300–13. https://doi.org/10.1016/j.carbon.2021.08.082.

[36] Nakajima Y, Murata H, Saitoh N, Yoshizawa N, Suemasu T, Toko K. Metal Catalysts for Layer-Exchange Growth of Multilayer Graphene. ACS Appl Mater Interfaces 2018;10:41664–9. https://doi.org/10.1021/acsami.8b14960.

[37] Castanheira L, Silva WO, Lima FHB, Crisci A, Dubau L, Maillard F. Carbon Corrosion in Proton-Exchange Membrane Fuel Cells: Effect of the Carbon Structure, the Degradation Protocol, and the Gas Atmosphere. ACS Catal 2015;5:2184–94. https://doi.org/10.1021/cs501973j.

[38] Bezerra CWB, Zhang L, Liu H, Lee K, Marques ALB, Marques EP, et al. A review of heat-treatment effects on activity and stability of PEM fuel cell catalysts for oxygen reduction reaction. J Power Sources 2007;173:891–908. https://doi.org/10.1016/j.jpowsour.2007.08.028.

[39] Shao-Horn Y, Sheng WC, Chen S, Ferreira PJ, Holby EF, Morgan D. Instability of Supported Platinum Nanoparticles in Low-Temperature Fuel Cells. Top Catal 2007;46:285–305. https://doi.org/10.1007/s11244-007-9000-0.

[40] Greeley J, Stephens IEL, Bondarenko AS, Johansson TP, Hansen HA, Jaramillo TF, et al. Alloys of platinum and early transition metals as oxygen reduction electrocatalysts. Nat Chem 2009;1:552–6. https://doi.org/10.1038/nchem.367.

[41] Conway BE. Electrochemical oxide film formation at noble metals as a surface-chemical process. Prog Surf Sci 1995;49:331–452. https://doi.org/10.1016/0079-6816(95)00040-6.

[42] Shinozaki K, Zack JW, Richards RM, Pivovar BS, Kocha SS. Oxygen Reduction Reaction Measurements on Platinum Electrocatalysts Utilizing Rotating Disk Electrode Technique: I. Impact of Impurities, Measurement Protocols and Applied Corrections. J Electrochem Soc 2015;162:F1144–58. https://doi.org/10.1149/2.1071509jes.

[43] Maillard F, Bonnefont A, Micoud F. An EC-FTIR study on the catalytic role of Pt in carbon corrosion. Electrochem Commun 2011;13:1109–11. https://doi.org/10.1016/j.elecom.2011.07.011.

[44] Maillard F, Schreier S, Hanzlik M, Savinova ER, Weinkauf S, Stimming U. Influence of particle agglomeration on the catalytic activity of carbon-supported Pt nanoparticles in CO monolayer oxidation. Phys Chem Chem Phys 2005;7:385–93. https://doi.org/10.1039/B411377B.

[45] Farias MJS, Camara GA, Feliu JM. Understanding the CO Preoxidation and the Intrinsic Catalytic Activity of Step Sites in Stepped Pt Surfaces in Acidic Medium. J Phys Chem C 2015;119:20272–82. https://doi.org/10.1021/acs.jpcc.5b05386.

[46] Giesen M, Beltramo G, Dieluweit S, Müller J, Ibach H, Schmickler W. The thermodynamics of electrochemical annealing. Surf Sci 2005;595:127–37. https://doi.org/10.1016/j.susc.2005.07.040.

[47] Asset T, Chattot R, Nelayah J, Job N, Dubau L, Maillard F. Structure–Activity Relationships for the Oxygen Reduction Reaction in Porous Hollow PtNi/C Nanoparticles. ChemElectroChem 2016;3:1591–600. https://doi.org/10.1002/celc.201600300.

[48] Moniri S, Van Cleve T, Linic S. Pitfalls and best practices in measurements of the electrochemical surface area of platinum-based nanostructured electro-catalysts. J Catal 2017;345:1–10. https://doi.org/10.1016/j.jcat.2016.11.018.

[49] Karuppannan M, Kim Y, Gok S, Lee E, Hwang JY, Jang J-H, et al. A highly durable carbon-nanofiber-supported Pt–C core–shell cathode catalyst for ultra-low Pt loading proton exchange membrane fuel cells: facile carbon encapsulation. Energy Environ Sci 2019;12:2820–9. https://doi.org/10.1039/C9EE01000A.

[50] Ohma A, Shinohara K, Iiyama A, Yoshida T, Daimaru A. Membrane and Catalyst Performance Targets for Automotive Fuel Cells by FCCJ Membrane, Catalyst, MEA WG. ECS Trans 2011;41:775–84.

[51] Imhof T, Della Bella RKF, Stühmeier BM, Gasteiger HA, Ledendecker M. Towards a realistic prediction of catalyst durability from liquid half-cell tests. Phys Chem Chem Phys 2023;25:20533–45. https://doi.org/10.1039/D3CP02847J.

[52] Antoine O, Bultel Y, Durand R, Ozil P. Electrocatalysis, diffusion and ohmic drop in PEMFC: Particle size and spatial discrete distribution effects. Electrochimica Acta 1998;43:3681–91. https://doi.org/10.1016/S0013-4686(98)00126-1.

[53] Takasu Y, Ohashi N, Zhang X-G, Murakami Y, Minagawa H, Sato S, et al. Size effects of platinum particles on the electroreduction of oxygen. Electrochimica Acta 1996;41:2595–600. https://doi.org/10.1016/0013-4686(96)00081-3.

[54] Stamenkovic VR, Mun BS, Arenz M, Mayrhofer KJJ, Lucas CA, Wang G, et al. Trends in electrocatalysis on extended and nanoscale Pt-bimetallic alloy surfaces. Nat Mater 2007;6:241–7. https://doi.org/10.1038/nmat1840.